Thermal and Statistical Models for Quench in Superconducting Cavities

Joshua Wiener, Hasan Padamsee, Laboratory for Elementary Particle Physics, Cornell University, Ithaca, New York, 14853, USA

Abstract

Previous computer models of defects in Niobium cavities have shown the dependence of breakdown fields on RRR and defect size [1, 2]. There is a need to expand upon these models to understand the large quantity of new data now available on 1-cell and multi-cell cavities and their quench fields [3]. A statistical analysis introduced by Safa [4] is adapted and carried out on quench field data of cavities prepared by EP, HPR and mild baking (such as the DESY 9-cell and 1-cell cavities), as well as for cavities prepared by BCP and HPR (such as CEBAF data on re-furbished 5-cell cavities). This analysis takes the simulated relationship between defect size and quench field to produce a defect probability distribution for a given set of cavities from their quench field data. In this way, the difference in performance between EP and BCP is cast in terms of different normal conducting defect sizes.

This study also shows some new and useful trends for reaching higher gradients. These new trends manifest themselves for small defects, which becomes the domain for gradients greater than 25 MV/m. We show that a higher phonon mean free path allows a 10% higher maximum field for very small (1 μm) defects. Lowering the helium bath temperature from 2 K to 1.6 K also improves the maximum field, but only when the phonon mean free path is large and the defect is small.

We also report the effects of the "non-linear" (enhanced) BCS resistance, Kapitza resistance changes, film boiling, high field Q-slope, residual resistance, cavity wall thickness, and rf frequency.

Simulation

The program simulates a cylindrical section of the niobium wall surrounding some circular defect of specified radius r and resistance R_d. The cylinder is 3mm in height, the typical thickness of the niobium, and 4mm in radius, with the defect in the center at the RF surface. The cross-section of this region is split up into a 2D mesh, each mesh element representing a ring around the central axis.

For each step of the simulation, the temperature of every mesh element is calculated using specified thermal conductivity and heat generation functions. There is a liquid helium bath on the bottom surface with temperature set to $T_b = 2.0$ K where heat may leak out of the cylinder. One can choose for heat to be allowed out of the sides of the cylinder or not. For most cases, turning this side heat flow on or off did not significantly change the results. All results shown here have no side heat flow.

Once the temperature of each element is calculated, the program finds the total absolute change in temperature across all of the elements. It also finds the total power produced on the RF surface as well as the total power emitted into the helium bath. The program continues to calculate new temperatures until the conversion criteria are reached. The total absolute change in temperature summed over all elements must be less than 0.0001 K and the difference between the created power and emitted power must be less than 0.1% of the created power. We then have thermal equilibrium and the temperature results are printed out. Figure 1 shows an example temperature profile for a 20 micron defect at the highest field before breakdown, with phonon mean free path $l = 0.2$ mm and $RRR = 300$. The temperature is stable. Note the log scale in the radial direction.

The mesh used is fixed but not linear. The grid density is high near the defect and low away from it to balance speed and accuracy (see Figure 2). The range along the central axis, normal to the RF and helium surfaces, is split up in an exponential fashion – the bottom half of the cylinder is one layer, the next quarter is the second layer, and so on, with a total of 13 elements along the axis. This results in the two elements nearest the defect having height less than 0.8 microns. For the radial direction, the defect radius itself is split up into four evenly spaced elements. The remainder of the radial range is split up quartically (the width of the ith element from the center is proportional to i^4), with 19 elements. The element just outside the defect has thickness less than 0.05 microns. This setup was found to be accurate in the sense that increasing the number of mesh elements did not appreciably change the results of the simulation.
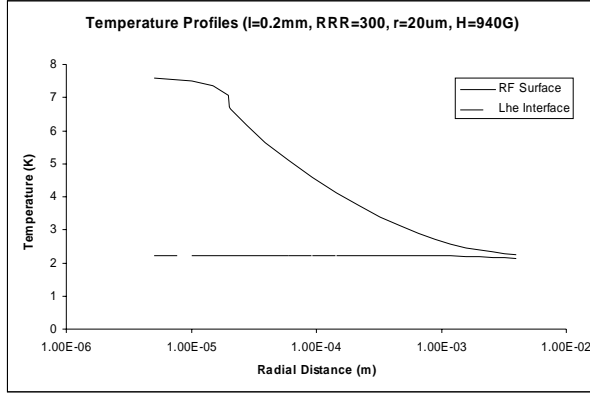
Figure 1: Temperature at the RF surface and liquid
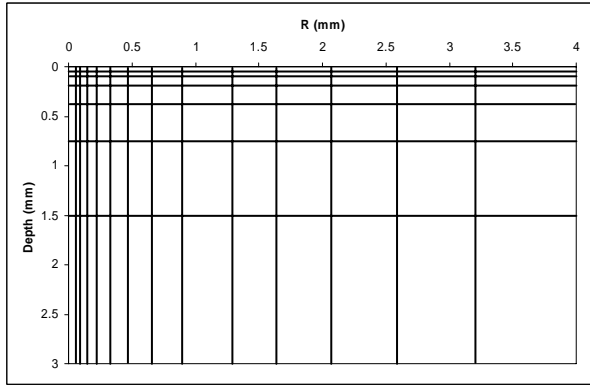helium interface around a 20 μm radius defect.

Figure 2: The 2D mesh. The defect is in the upper left
corner. Gridlines closest to the edges are not shown.

For a given set of parameters (defect size, *RRR*, phonon mean free path, etc.) the maximum field was determined by finding the highest field for which the temperature of the element adjacent to the defect on the RF surface was less than the field-dependant critical temperature. In other words, we find the highest field where all the niobium on the RF surface stays superconducting. We can then look for trends of the maximum field with various parameters.

Surface Resistance

The amount of heat generated at the RF surface depends on the resistance of the niobium. The defect is always considered normal conducting and is assigned a resistance of 0.01 Ω. This is a very simple assumption. Real defects may have a large range of resistances, and therefore a larger range of sizes. In a later section we explore the scaling relationship between defect resistance and equivalent defect size.

For the rest of the RF surface, the simulation uses an approximation of BCS resistance:

$$R_{BCS} \approx 1.6 * 1.61x10^{-4}\left(\frac{f}{2.856}\right)^2 \frac{1}{T}\log\left(16T\frac{2.856}{f}\right)e^{-Y}$$

Above, *f* is the frequency and *Y* is

$$Y = \frac{17.205}{T}\sqrt{\cos(.0184T^2)}$$

Thermal Conductivity

We plan to examine the effect of phonon mean free path on the quench field, i.e. the influence of the phonon peak. Cavities annealed at high temperatures and cavities from large grain material have phonon peaks of various magnitudes. Accordingly, the program uses the thermal conductivity function of [5] which depends on the RRR and the phonon mean free path. Figure 3 shows the resulting thermal conductivity curves with four values of phonon mean free path *l* ranging from 1 mm to 10 mm, all with *RRR* = 300.
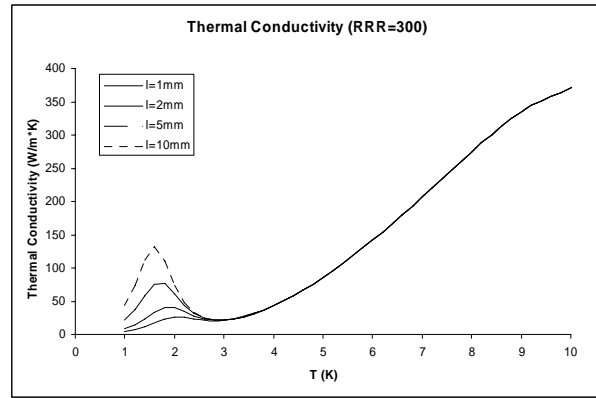

Figure 3: Bonin thermal conductivity with different
values of phonon mean free path *l*.

Simulation Results

Shown in Figures 4 and 5 are the baseline results obtained with *l* = 0.2 mm (no phonon peak in the thermal conductivity), bath temperature T_b = 2.0 K, standard BCS resistance, fundamental critical field of 2000 G at zero temperature, and no high-field Q-slope. Figure 4 plots the breakdown field versus defect size for various RRR values, and Figure 5 shows breakdown field versus RRR for various defect sizes. A 300 RRR TESLA-shape cavity (Hpk/Eacc = 42 G/MV/m) which quenches at 20 MV/m is likely to have a normal conducting defect of radius about 20μm dropping to 5 μm radius at 30 MV/m. These numbers pose a significant challenge to optical inspection techniques when the goal is to reach 35 MV/m.

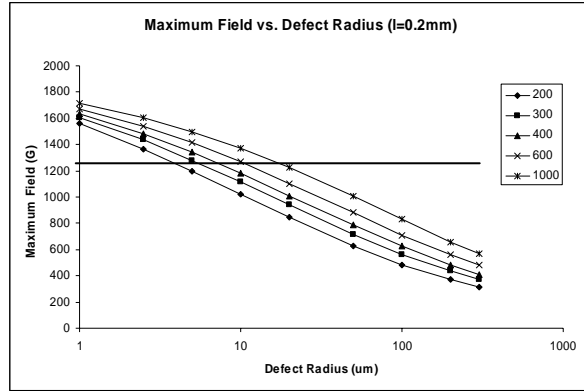**Maximum Field vs. Defect Radius (l=0.2mm)**

Figure 4: Quench field vs. defect size.
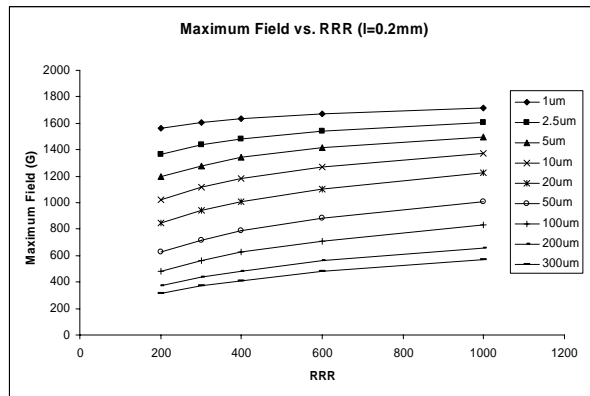
Maximum Field vs. RRR (l=0.2mm)

Figure 5: Qunech field vs. RRR.

Note that the vertical axis here is linear so that the breakdown fields do not appear to saturate as fast as they appear to on the log plot of [1]. We also do not know all the detailed parameters of the previous simulations [2] for a detailed comparison, but the result here are in rough agreement.

Critical Field

The base simulation uses a critical field of 2000 G. Raising this to 2200 G significantly improved the quench fields for small defects (e.g. 1 μm), from 1600 G to 1750 G, as shown in Figure 6. In the high field range, only possible if defects are small, the critical field is also more sensitive to changes in bath temperature. A zero temperature critical field of 2300 G with a bath temperature of 1.8 K shows the quench field for 1 μm defects to rise to 1800 G.
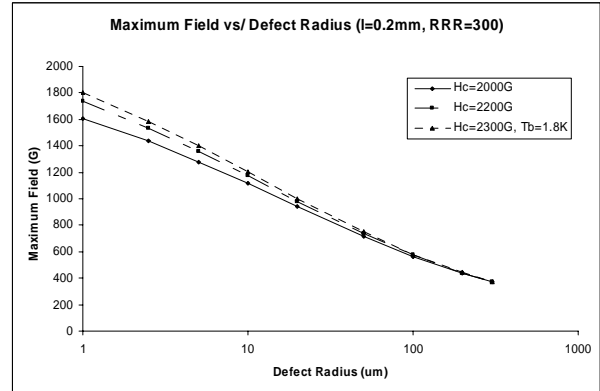
Maximum Field vs/ Defect Radius (l=0.2mm, RRR=300)

Figure 6: Comparison of quench fields for different zero temperature critical fields.

Statistical Analysis of Defects and Quench Fields

An analysis introduced by H. Safa [4] allows us to use the defect size vs. quench field simulation along with cavity data on quench field distribution to translate observed quench field statistics into defect statistics. The process is as follows.

Let $p(r, S)$ be the probability that all defects on an area S of niobium have radius less than r. First, note that $p(r, 2S) = [p(r, S)]^2$ since an area of $2S$ can be split up into two areas with area S. This means $p(r, S)$ is exponential in S. Additionally, $p(r, S)$ must be monotone increasing with r, approaching 1 as r gets larger and 0 as r nears 0. From these features, Safa assumes a general form of

$$p(r, S) = \exp[-(S/S_0)(r_0/r)^m].$$

The value of S_0 is arbitrary and serves as a way to normalize the cavity area. In all of the following, S_0 is set to the area of a single-cell 1.3 GHz cavity. The values of r_0 and m determine the shape of the curve, which might look something like figure 7.
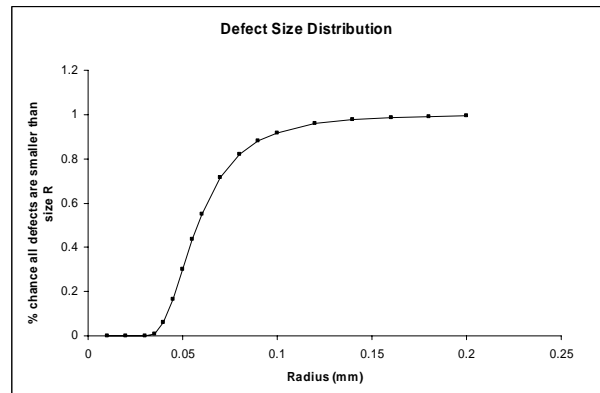
Defect Size Distribution

Figure 7: A possible defect distribution of the form shown above.

The probability distribution for the quench field can be compared and fit to existing quench field data by adjusting the r_0 and m values as in Figure 9 (see the success rate version of this same histogram in Figure 10). Once these values are fixed, we substitute r back in, and now we have a probability distribution of largest defect size which corresponds to the quench field data (Figure 11).

If a cavity has no defects of size greater than r, then from the simulation we know it has a quench field of at least some magnetic field $B(r)$. By making an explicit fit (Figure 8) of the inverse of this relationship, we can substitute $r(B)$ into $p(r, S)$ and obtain a probability distribution of quench fields $p(B, S)$. (In Figure 8 the base simulation with $l = 0.2$ mm and $RRR = 300$ is fit with a logarithmic r-dependence.) This fit procedure can used to translate data for quench field probability distributions for a set of cavities to a defect probability distribution by adjusting the r_0 and m values.

For example, Figure 9 displays the 9-cell cavity <u>quench</u> probability distribution data from 66 tests with 51 cavities. We do not distinguish results between different batches and suppliers. For these tests the cavities were all prepared by EP/HPR and showed quench as the gradient limitation. Most of the cavities were baked at 120 – 130 C for about 48 hours (mild bake). This is the standard treatment now in practice for high gradients. In a few tests (about 12), cavities which were not baked were also included in the set of quench data because these showed quench (with Q > 10^{10}) before reaching the high field Q-slope region. The rationale is that baking is used primarily to eliminate the high field Q-slope, not the quench. If the cavity quenched below the high field Q-slope regime, it is expected that the baking would not improve the quench field. Cavities which were treated by EP followed by flash BCP (10 μm) were also included in this overall data set with the rationale that the EP/flashBCP behavior is predominantly influenced by the main EP treatment. We also included two tests without quench above 35 MV/m as these tests would fall into the highest gradient bin in any case. For more details on the data used, see the last Section and the Appendix Tables A and B.

Figure 10 re-plots the measured quench probability distribution of 66 tests as gradient yield. 75% of 9-cell DESY cavities reached 25 MV/m without quench and 20% reached 35 MV/m without quench.

Defect Distributions for 9-cell EP Cavities

To cast these quench distributions in terms of defect size distributions, the values of r_0 and m are determined to provide defect probability distributions (Figures 11 and 12). Figures 9 (and 10) show the fits between the observed and predicted quench probability (and yield)

distributions obtained. The defect distribution corresponding to the chosen r_0 and m values is shown in Figure 11 which may be better understood as a probability density. For example there is a 90% probability that defects on EP/HPR/baked cavities are less than 20μm radius, and there is a 50% probability defects are less than 5 μm radius. Such defects in high performance cavities may be rather difficult to detect using optical inspection in a 9-cell unit.

To describe the distribution differently, Figure 12 shows the probability density of the largest defect on the 9-cell cavity. The chance that the largest defect has radius in the range $[R, R+\Delta R]$ is $\Delta R * \partial p / \partial r(R)$. For example, the probability that the largest defect is 20 μm (radius) is about 1% and the probability that the largest defect is 2 μm is 18% at the peak in the probability distribution. However if the defect has a surface resistance less than the normal state the size may be larger in order to deposit the power necessary to reach quench, as we will discuss later. By comparison with Figure 9, which shows the maximum occurrence (35%) at 30 – 35 MV/m, we may expect that defects in most of these high performance cavities are very small (i.e., 2 μm radius).
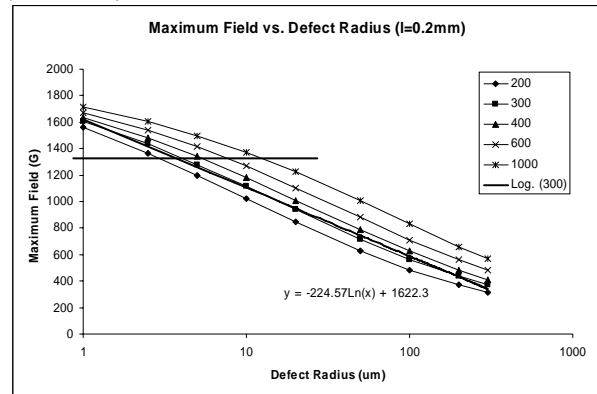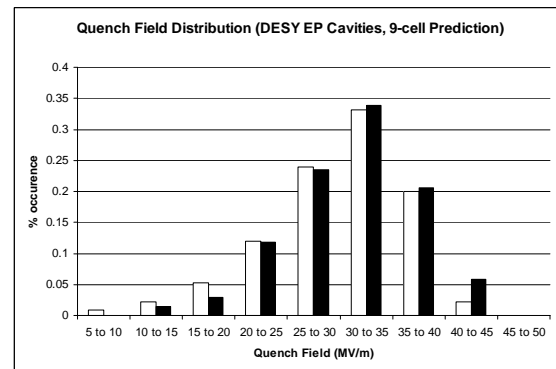

Figure 8: A logarithmic fit of the base simulation.

Figure 9: Quench distribution compiled from DESY data base on cavities treated with EP/HPR and bake. <Eacc> = 30.8 ± 5.8 MV/m. The dark bars are data and the white bars are from the simulation.
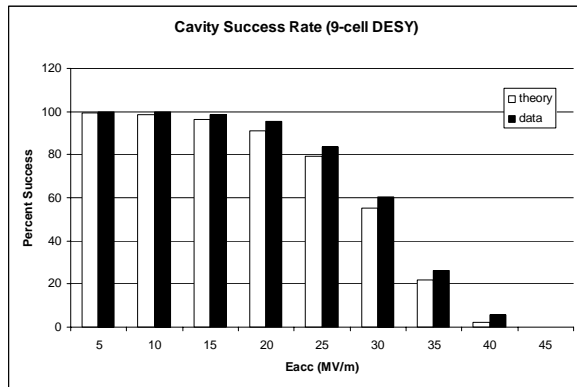
Cavity Success Rate (9-cell DESY)

Figure 10: Observed success rate with matched theoretical probability for 9-cell DESY EP cavities.

Defect Size Distribution (9-cell DESY cavities)
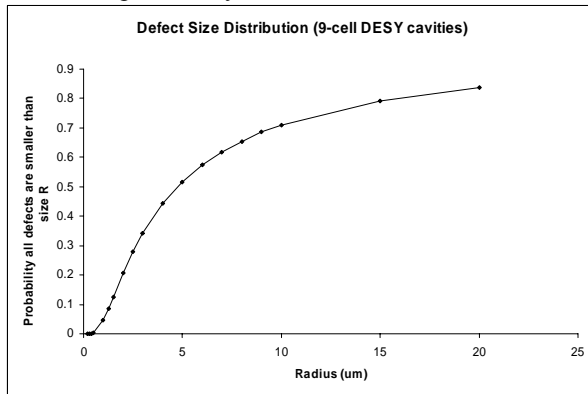
Figure 11: Defect probability for 9-cell DESY EP cavities.
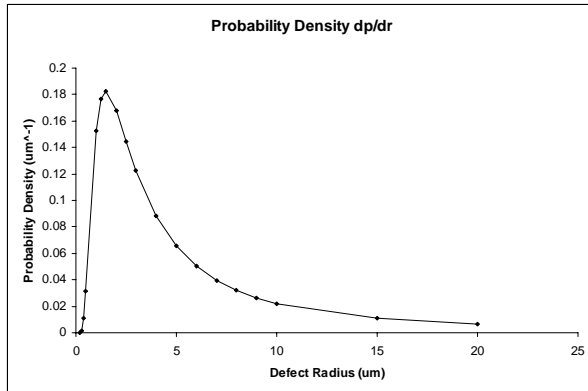
Probability Density dp/dr

Figure 12: Probability density of the largest defect radius. The peak is near 2 μm.

Defect Distributions for 1-cell EP Cavities

Suppose we use the same parameters r_0 and m to calculate what will be the gradient distribution for single cell cavities prepared by EP/HPR and bake. This is done simply by reducing the area S in the probability formula by a factor of 9 while keeping everything else the same. Then we obtain the calculated result of

Figures 13 and 14. Therefore the yield of single cell cavities will be over 80% for E_{acc} > 35 MV/m. This simple simulation quantifies the area effect and shows how high yield results from single cell cavities should be carefully weighted by the area factor. The big difference in yield between Figure 10 (9-cells) and Figure 14 (1-cell) for the same cavity preparation should caution us not to derive too much comfort from any high yield single cell results per se. Of course comparisons between single cell results for two kinds of treatments are always meaningful and helpful.
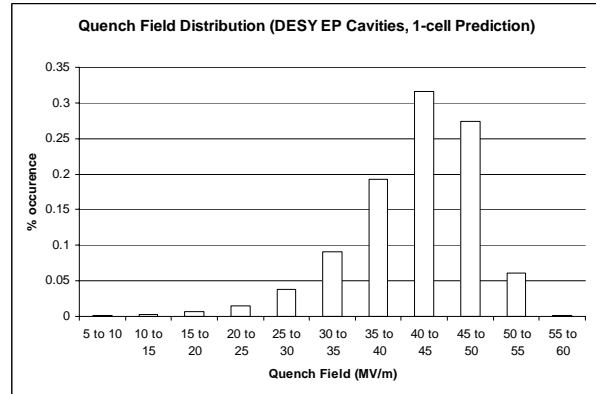
Quench Field Distribution (DESY EP Cavities, 1-cell Prediction)

Figure 13: Predicted 1-cell quench field distribution.

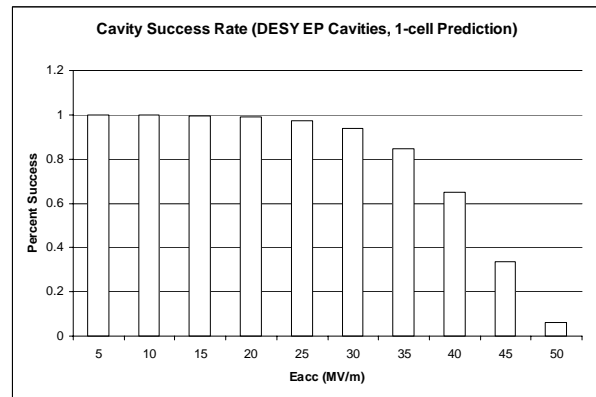**Cavity Success Rate (DESY EP Cavities, 1-cell Prediction)**

Figure 14: Predicted 1-cell cavity success rate.

Quench and Defect Distributions for BCP Cavities

A second data set consisting of 1.5 GHz 5-cell BCP treated CEBAF cavities is shown in Figure 15 [6]. The square points (pink) are quench limited tests only, and were put into a histogram of quench fields. The re-furbishing tests were reported to be free of field emission. The corresponding success rate histogram with theoretical fit is shown in Figures 16 and 17. The defect distribution and probability densities are shown in Figures 18 and 19. The peak defect size is around 50 μm radius, much larger than the peak found in the DESY EP data set. To fit the CEBAF data we used H_{pk} = 47 Oe/MV/m as contrasted with H_{pk} = 42 Oe/MV/m

for the TESLA-shape DESY cavities. For reasons yet to be understood, BCP preparation gives higher defect radii than EP preparation. It is also possible that the defects are similar for EP and BCP treated cavities, but the field enhancement from the higher surface roughness of the BCP treatment lowers the quench field.

A third data set was collected which included 9-cell BCP treated DESY cavities with no heat treatment higher than 800°C. See Appendix B for a list of cavity tests. The data set is sparser than for the CEBAF BCP data, since DESY used 1350C Ti-treatment plus BCP for most of the BCP prepared cavities. The success rate and probability density for this data set are shown in Figures 20 and 21. Most of the Q values in this data set are higher than 6×10^9, so that the Q-slope probably does not play a role in the quench field. Two data points (without quench) above 30 MV/m have been included and these cases are no doubt dominated by the Q-slope. However the data show that the quench field for these two tests is still above 30 MV/m, and so it is most likely safe to place these in the highest bin (30 – 40 MV/m).

The defect distributions for BCP DESY data show that the peak defect size is about 10 μm, which is a big surprise when compared to the quench data of BCP re-furbished CEBAF cavities (peak defect radius = 50μm). The Nb material for the DESY cavities was obtained 5 to 10 years later than the CEBAF Nb, and the DESY sheets were individually scanned with eddy current to eliminate possible large defects. Hence it is encouraging to see the most probable largest defect size fall from 50 μm to 10 μm. However eddy current scanning only rejects a small percentage of the starting sheets, so it may not play a large role. Another possibility is improvement in weld quality over time.
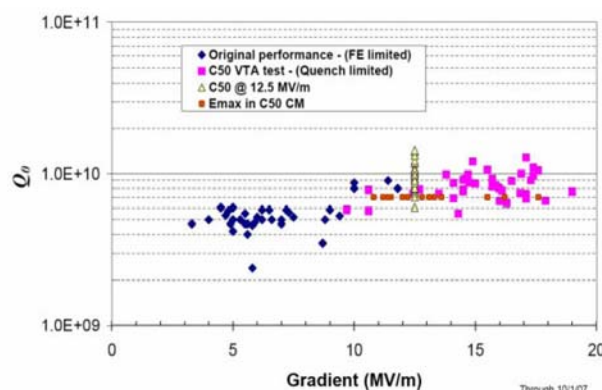
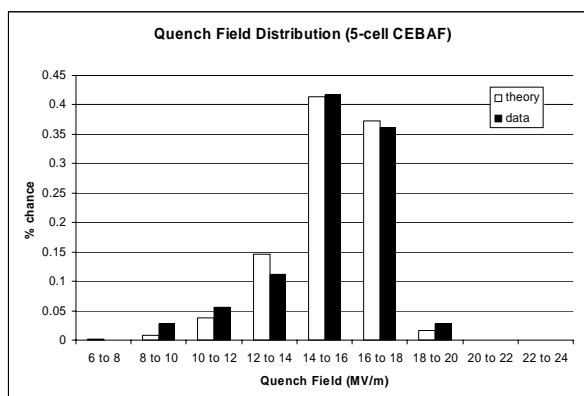Figure 15: CEBAF cavity test quench data. <Eacc> = 15.2 ± 2 MV/m, H_{pk} = 47 Oe/MV/m.

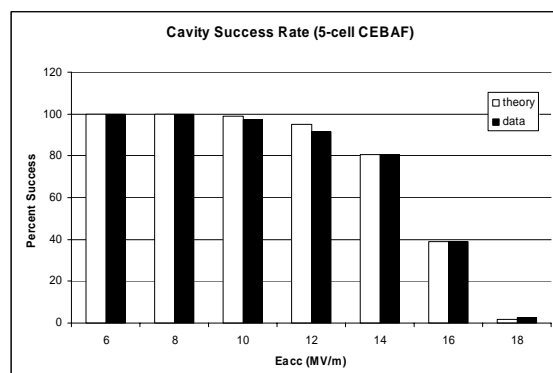Figure 16: CEBAF quench field distribution.
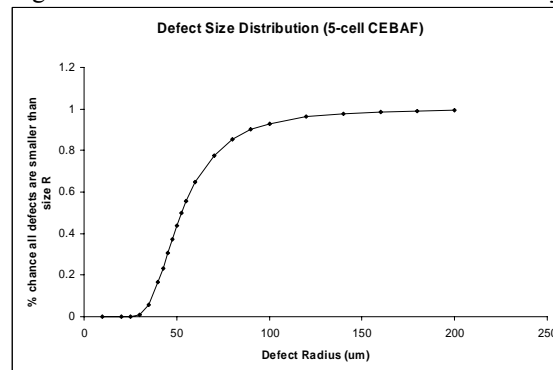
Figure 17: CEBAF data set success rate with theory.
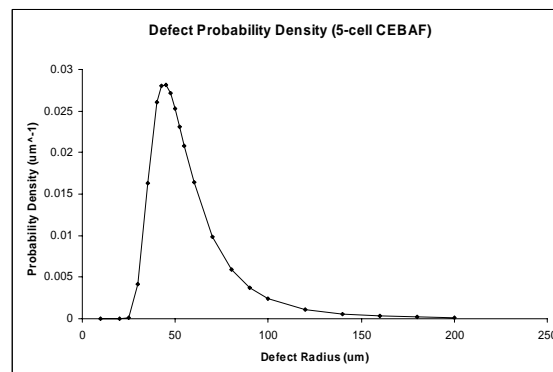
Figure 18: CEBAF defect probability distribution.
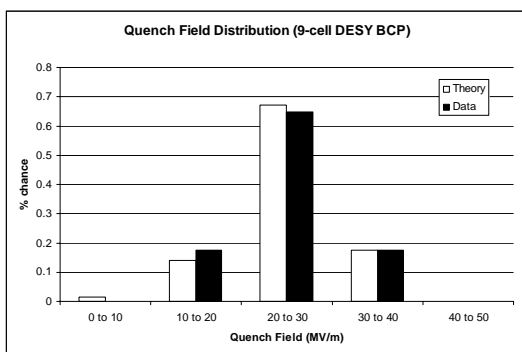
Figure 19: CEBAF defect probability density.

Figure 20: BCP DESY data set quench distribution. <Eacc = 25.1 ± 4.4 MV/m. Cavities/tests with post-purification at 1350 C are excluded.
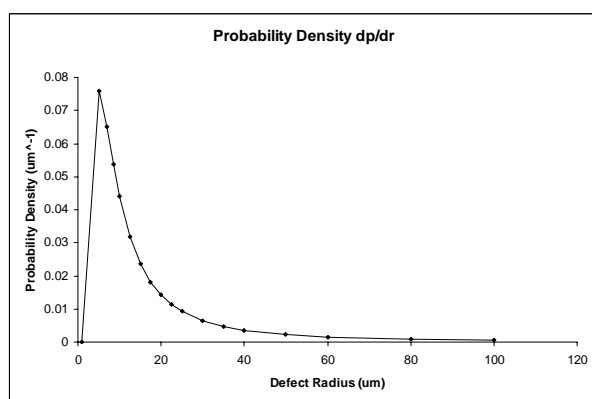

Figure 21: BCP DESY cavities defect probability density.

New Results from the Thermal Model

This study shows new and useful trends for reaching higher gradients. These new trends manifest themselves for small defects, which becomes the domain for gradients greater than 25 MV/m. We show that a higher phonon mean free path allows a 10% higher maximum field for very small (1 μm) defects. Lowering the helium bath temperature from 2 K to 1.6 K also improves the maximum field, but only when the phonon mean free path is large and the defect is small.

We also report the effects of the "non-linear" (enhanced) BCS resistance, Kapitza resistance changes, film boiling, high field Q-slope, residual resistance, cavity wall thickness, and rf frequency.

Phonon Mean Free Path

With the arrival of large grain and single grain Nb cavities there has been some interest in whether the phonon peak (Figure 3) in the thermal conductivity helps to stabilize the quench. In the absence of grain boundaries phonons start to play a major role in heat conduction when the temperature falls below 2.5 K and the number of normal conducting electrons (scattering phonons) drops to a very low value due to pair condensation.

We determined quench fields for a range of values between l = 0.1 mm and l = 10 mm with *RRR* = 300 Nb and bath temperature of 2 K. As Figure 22 shows, there is no change in the quench field across this entire range unless the defect radius is less than 10 microns. But even the smallest defect of radius 1 micron shows a difference of less than 100 G in the max field between the l = 0.2 mm case and the l = 10 mm case.
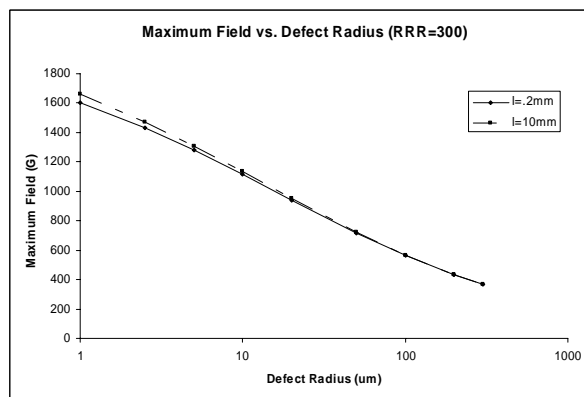
Figure 22: Comparison of low and high phonon mean free path at RRR=300

The reason that the phonon peak in the thermal conductivity does not help to stabilize the defect is that the temperature outside the defect rises to 3 K so that the phonon peak plays no role in diffusing the heat away from the defect. Figure 23 shows the temperature profiles at the RF surface at a field near quench for two values of l for a 1 micron defect. Figure 24 shows the temperature profiles for a 20 micron defect.

Since the phonon peak is maximum at about 1.6 K we also studied in the next section the influence of bath temperature on quench field with and without the phonon peak.

Figure 23: Temperature profile comparison of small l and large l for a 1 μm defect.

Figure 24: Temperature profile comparison of small l and large l for a 20 μm defect.

Helium Bath Temperature

The bath temperature was set to 1.6 K, 1.8 K, and 2.0 K with *RRR* = 300 and *RRR* = 1000. We found no change with bath temperature in quench fields for l = 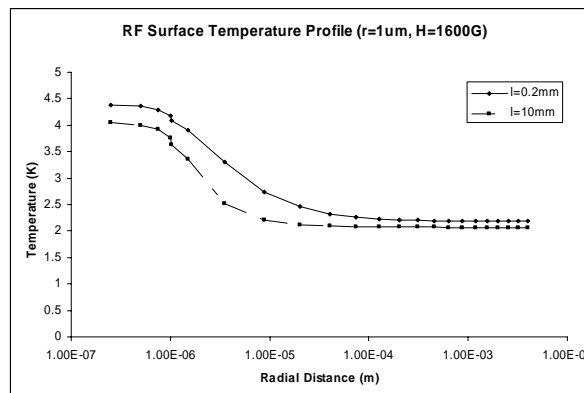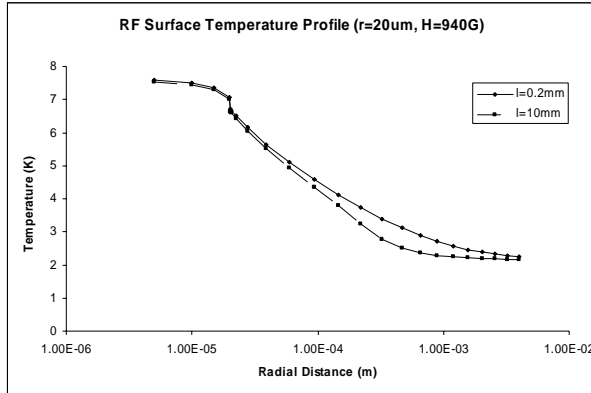0.2 mm for any defect size. For large phonon mean free path, l = 10 mm, changes *were observed* for defects below 10 microns radius (Figure 25). Max fields for the smallest defect size (1 micron) are as much as 140 G (about 3 MV/m) higher for T_b = 1.6 K than for T_b = 2.0 K. The increase is larger for smaller defects, and the difference between 1.6 K and 1.8 K is larger than between 1.8 K and 2.0 K. This may well be explained by the 1.6 K peak in the thermal conductivity function.
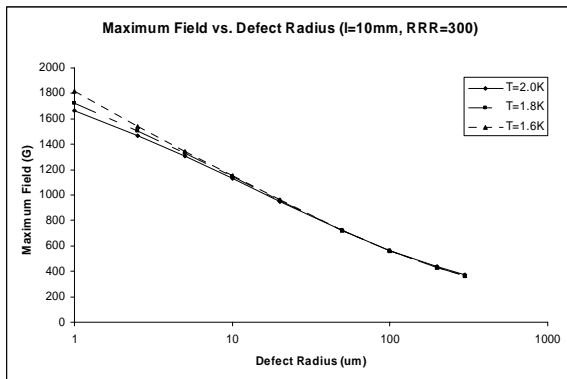

Figure 25: Comparison of two different bath temperatures. Smaller defects see a larger difference.

Non-Standard BCS Resistance

Recently Gurevich [7] has shown that the BCS resistance needs to be modified in the presence of a surface RF magnetic field. His non-standard BCS resistance (or non-linear as it is called) was also used to study the influence on quench without defects. This non-standard resistance is equal to the BCS expression multiplied by a polynomial in β_0, where

$$\beta_0 = \frac{\pi}{2^{3/2}} \frac{H}{H_c} \frac{\Delta}{k_B T} = \frac{\pi}{2^{3/2}} \frac{H}{H_c} \left(\frac{\Delta}{k_B T_c} \right) \frac{T_c}{T}$$
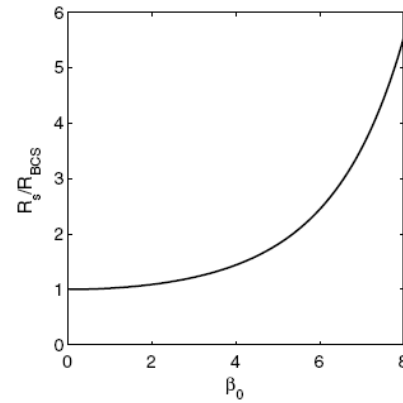

Figure 26: The multiplicative change in resistance as a function of β_0. Graph from Gurevich [7].

The quantity in parentheses is a constant roughly equal to 1.92. The dependence of this polynomial on β_0 is shown in figure 26. Note that β_0 must be above 6 for R/R_{BCS} to exceed 2.

Incorporating the non-standard BCS resistance did not affect the maximum fields except for the smallest size defects (see Figure 27). Even for small defects, there is only a 60G decrease due to non-linear resistance. This is likely due to the fact that at temperatures near T_c the value of β_0 is low, and so the non-standard resistance is close to the standard BCS resistance.

For the very small defect cases there is much more heat produced over the entire RF surface with the Gurevich enhancement (see Figure 28). This was checked for *RRR* = 300 and *RRR* = 1000, l = 0.2 mm and l = 10 mm. Therefore only the low temperature high field cases are affected to a small degree.

Film Boiling

If the outward heat flux of any mesh element on the helium interface exceeds a threshold value (1 W/cm^2), we declare film boiling to be in effect and reset the heat flow of that element into the helium bath to zero. This greatly limits the maximum fields for large defects, where there is more heat produced. Figure 29 shows the effect of film boiling on cavities with RRR = 300 and RRR = 1000. For defect radii larger than 100 μm, there is little dependence of quench field on RRR. Film boiling becomes the primary limitation for large defects.
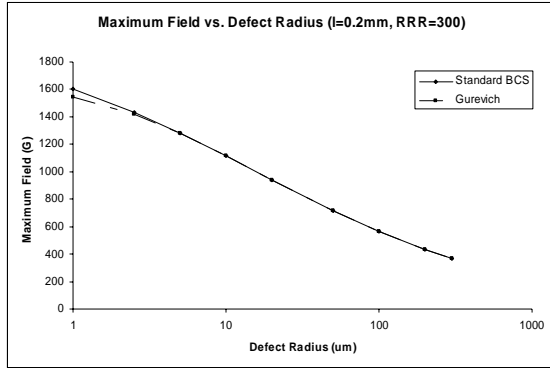
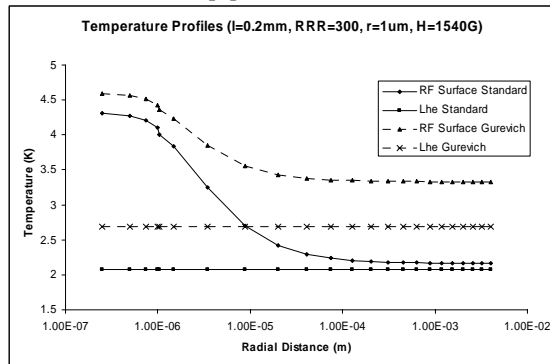Figure 27: Comparison of BCS resistance to Gurevich [7] resistance.

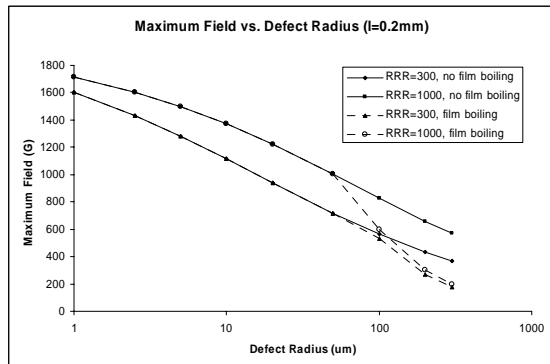Figure 28: Temperature profiles for the Gurevich [7] resistance simulations are hotter.

Figure 29: The effect of film boiling on RRR = 300 and RRR = 1000 niobium.

Kapitza Resistance

Since the Kapitza resistance is very sensitive to the detail surface condition it is interesting to examine how strongly it influences the quench field for large variations. The Kapitza resistance can vary by large amounts depending on the outside wall condition. Simulations were run with 10 times normal and 1/10 the normal Kapitza resistance. The results are shown in Figure 30.

Decreasing the Kapitza resistance showed no appreciable improvement in the quench fields for the full range of defect sizes studied. The insensitivity is because the quench field is determined primarily by the heat flow conditions near the defect which depend mostly on the local thermal conductivity. However, increasing the Kapitza resistance by a factor of 10 lowers the quench field by a large amount (30%) for defects smaller than 10 μm radius, as shown in Figure 30. The higher Kapitza resistance prevents heat from escaping through the bottom. The heat from the defect is thus forced to the sides which increases the BCS resistance on the RF surface and produces more heat.

Since we are aiming for consistent gradients above 30 MV/m where the defect size is smaller than 10μm, we must not neglect the cleanliness of the outside surface of cavities in the efforts to reach the highest possible gradient.

Residual Resistance

All simulations discussed so far included a residual resistance of 10 nΩ. However, changing this value by a factor of two to 5 nΩ and 20 nΩ caused no change in the quench fields. Even changing by a factor of 10, to 1 nΩ and 100 nΩ, had little effect. The heating due to residual resistance is very small compared to the heating due to the normal conducting defect.
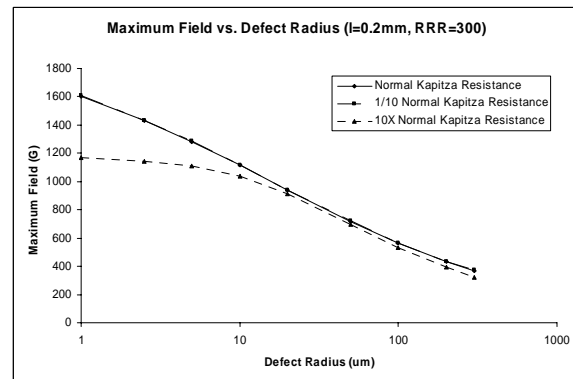
Figure 30: The effect of a large Kapitza resistance on the quench field.

High Field Q-Slope

Cavities prepared by BCP or EP without the mild bake show a strong high field Q-slope above 90 mT. We examine the influence of high field Q-slope on the quench field. An empirical approximation of high field Q-slope is included in the simulation as an option (off by default) via a field-dependant "extra" resistance R_{ex} which is added to the RF surface resistance for the sole purpose of lowering Q in the high field range. A collection of non-baked BCP treated 9-cell cavities from the DESY database which exhibited high field Q-slope was used to determine this extra resistance

(Figure 31). We assume an exponential form for the field dependence:

$$R_{ex} = A*\exp(B*E_{acc}).$$

The resulting quality factor was calculated using

$$Q = 270/(R_{ex} + R_{bcs} + R_{res}),$$

where R_{res} is the extra residual resistance of the niobium. The zero field residual resistance is set to 10 nΩ. For the purpose of this fit, a value of 10 nΩ was also used for R_{bcs}, corresponding to a temperature of just over 2 K. The parameters A and B were then adjusted to visually simulate the data of Figure 31. A number of pairs of values were used that put the Q curve somewhere within the range of the data. One such fit is shown in figure 31. Note that the fit at low fields is not affected by A and B but rather depends on the residual resistance and BCS resistance.

Figure 31: Fit of Q vs. E. The solid line is the fit. See appendix for a list of tests used in the data.

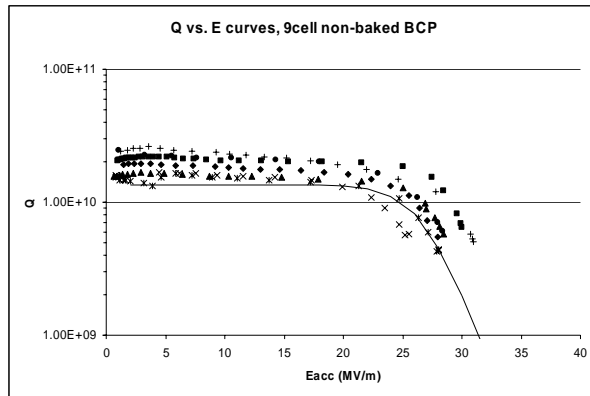Implementing the simulated high field Q-slope, we find that the quench fields for small defects are significantly lowered. The effect is greater for higher RRR as fields approach the high field Q-slope regime (see Figure 32). The simulation shown here corresponds to the particular Q-slope fit shown in Figure 31. Implementing the high field Q-slope also eliminates nearly all the dependence of the quench field on the phonon mean free path, *l*. If we also include film boiling, we see an even lower ultimate quench field of around 1425 G (~34 MeV), as seen in Figure 32. The limit is sensitive to the two Q-slope parameters A and B. For all pairs that we used to simulate the range of the high field Q-slope, the ultimate field falls between 30 and 35 MV/m. Hence the high field Q-slope for BCP cavities provides a good reason for the saturation in quench field near 30 -35 MV/m as seen in the DESY data of Figure 33 [8].
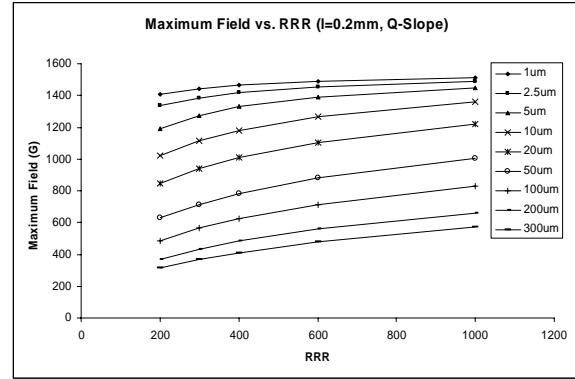
Figure 32: Simulations for high field Q-slope. Separate curves are shown for various defect sizes.
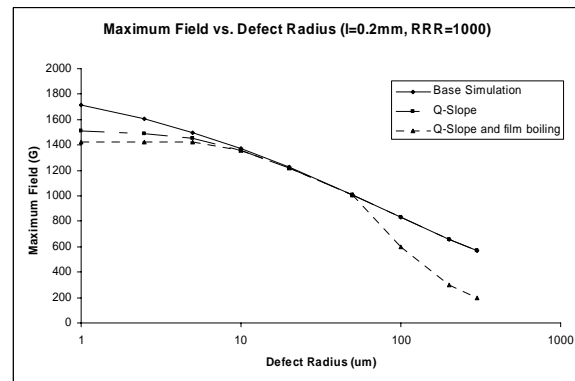
Figure 32: Implementing high field Q-slope has a large effect on the best performing simulations.
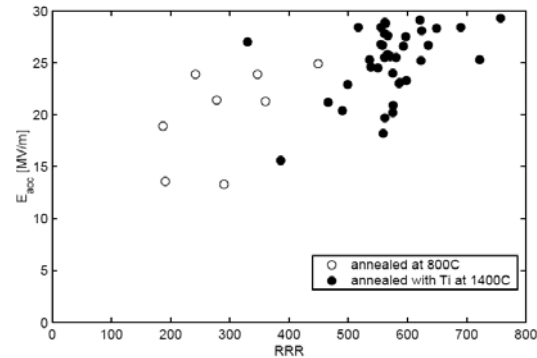
Figure 33: Maximum field for BCP prepared cavities. Many cases are limited by quench.

RF Frequency

Three frequencies (0.8 GHz, 2.4 GHz, 4.0 GHz) were simulated in addition to the base frequency of 1.3 GHz. The results for 0.8 GHz are unchanged from the 1.3 GHz results (Figure 34). The 2.4 GHz and 4.0 GHz tests had much lower quench fields for small defects, as seen in figure 26. If film boiling is turned on, the quench fields in this range are further reduced (see Figure 27), which suggests that large RF heat losses are causing the decreased performance for the higher frequencies.
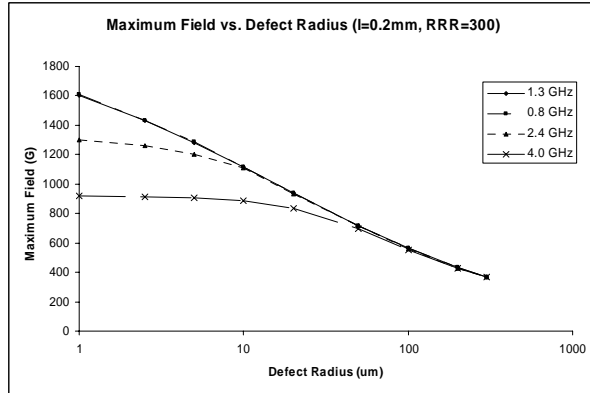
Figure 34: Quench fields vary greatly with frequency for small defects.
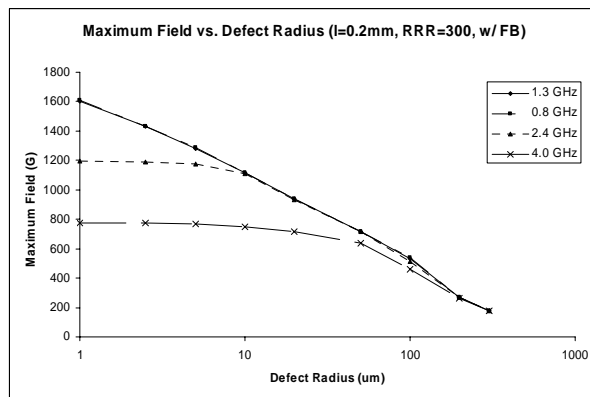
Figure 35: The high frequency cases produce so much RF heating that they are limited by film boiling.

Scaling Law for Defect Resistance and Defect Size

So far we have only treated defects with the full normal conducting resistance (~10^{-2} Ω). However we know very little about the nature of defects that exist on the cavity surface. What is the impact of a defect with smaller resistance? We address how to treat a low resistance defect in terms of the "equivalent defect size" of a normal conducting defect. We find that it is not appropriate to use the simple scaling law (i.e. defect size ~ $\sqrt{}$defect resistance) suggested by the equivalent power flow into the defect. The main reason is that reducing the size of the defect to absorb the same power as the lower resistance defect also affects the relative heat flows out of the sides and the bottom of the defect.

We used the simulation to analyze the heat flowing out of the defect in the following way. We recorded the heat flux out of the sides and bottom of the defect for a fixed field of 500 G. The mesh elements which were considered to comprise the defect were the innermost four mesh elements on the single topmost layer. We varied defect size with constant defect resistance, varied defect resistance with constant defect size, and varied both with constant defect power deposited. The

thickness of the defect was kept the same – only the radius is varied, as per the chosen 2D mesh. We find that the distribution of the heat flow out of the sides and bottom of the defect depends on the parameters of the defect.

The results show that the percent of defect-produced heat which flows out the side of the defect is roughly the same as the percent of the surface area of the defect taken up by the sides. That is, the distribution of emitted heat depends only on the size of the defect, and not on the defect resistance or total power emitted (see Figure 36).
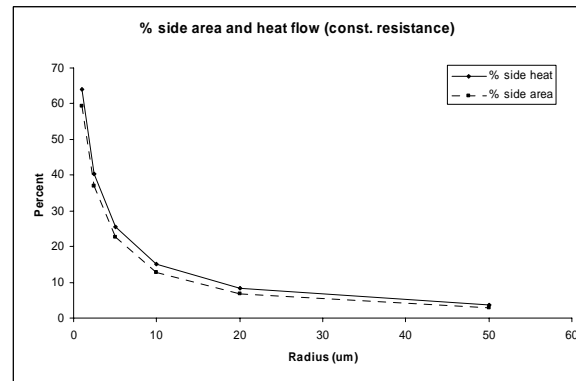
Figure 36: Percent side heat and side area.

One consequence is that, since the side heat flow plays a major role in determining the quench, a cavity with a defect of size r and resistance R_d will have the same quench field as one with a defect of size $10r$ and resistance $R_d/10$. This second defect will have 10 times the total power output (power goes as $r^2H^2R_d$) but the percent side area is roughly 10 times lower. The side heat flow is therefore nearly the same as in the first case, resulting in the same quench field. This can be seen in Figure 37, where we compare the base simulation to a simulation with 1/10 the defect resistance. See that reducing the resistance by a factor of 10 corresponds to decreasing the radius by a factor of 10, seen as a uniform shift of the graph on this semi-log plot.
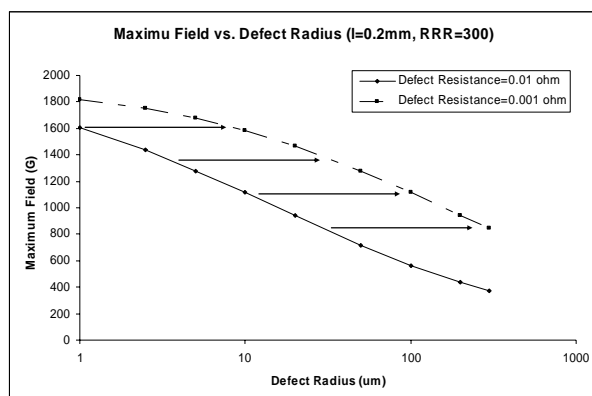
Figure 37: Quench fields of defects with 1/10 the usual resistance, compared to the base simulation.

Conclusions

With the new surface treatment of EP/HPR/bake replacing the old treatment of BCP/HPR, the average quench field has increased from 25 to 31 MV/m. Both treatments include 800 C annealing for 2 hours primarily for H gas removal. The improvement between the EP and BCP sets corresponds to a shift in the peak of the defect size distribution from to 10 μm to 2 μm defect radius. For the EP treated cavities about 50% of the defects are smaller than 5 μm radius and almost 90% defects are smaller 20μm radius. Why EP treatment results in such small effective defect size is not yet clear.

The above results are manifest from DESY EP tested cavity performance. The BCP treated DESY cavities show a peak defect radius of 10 μm. These cavities also show higher quench fields than the CEBAF re-furbished cavities which have been prepared by 600 bake, BCP/HPR. For the CEBAF set of BCP treated cavities the quench field is nearly 50% lower. Perhaps the higher quench field for the DESY cavities can be attributed to improvements in material quality over the 5 – 10 intervening years, as well as to the benefits of prior eddy current screening of the sheets for the DESY cavities. However eddy current scanning only rejects a small percentage of the starting sheets, so it may not play a large role. Another possibility is improvement in weld quality over time.

The phonon mean free path and helium bath temperature do affect the breakdown fields due to defects on the RF surface, but have less impact than defect size and *RRR*. Additionally, these only have noticeable effects on high *RRR* cavities with small defects. There is little observed difference in breakdown fields between the standard and non-standard BCS resistances, but the non-standard version runs hotter at very high fields.

Film boiling is an important limitation for large defects, and puts an absolute limit on the accelerating field for cavities with high field Q-slope. Kapitza resistance has a large effect on the quench field for small defects, and affects the film boiling limit for large defects. RF frequencies higher than 2 GHz have drastically lower quench fields for small to medium size defects.

References

[1] H. Padamsee et al. *A Statistical Model for Field Emission in Superconducting Cavities,* Proceedings of the 1993 Particle Accelerator Conference, Washington DC, p. 998 (1993).

[2] D. Reschke *Limits in Cavity Performance* 2007 SRF Workshop Tutorial.

[3] TESLA Technology Collaboration Cavity Database, RF Tests: *http://teslanew.desy.de/cavity_database/rf_tests/index_eng.html*

[4] H. Safa *Statistical Analysis of the Quench Fields in SCRF Cavities*, Proceedings of the Eighth Workshop on RF Superconductivity Vol III Abano Terme, Italy, 1997

[5] F Koechlin and B Bonin, "Parametrization of the Niobium Thermal Conductivity in the Superconducting State," Supercond. Sci. Technol. 9, 453 (1996).

[6] J. Preble, "CEBAF Energy Upgrade Program Including Re-Work of Cebaf Cavities," J. Preble, Proc., 13th Workshop on RF Superconductivity, Beijing, China, paper FR104 (2007).

[7] A. Gurevich *Multiscale Mechanisms of SRF Breakdown*, Physica C 441 (2006) 38–43

[8] B. Aune, et al, "Superconducting TESLA Cavities," Phys. Rev. ST AB, 3, 092001 (2000).

Appendix A – List of DESY EP treated cavity tests *http://teslanew.desy.de/cavity_database/rf_tests/index_eng.html*

Cavity	Etch depth (mm)	Heat Treatment	Temp	Date test	MV/m Emax	Q	Limit
A16	343.8	ep, b	1350	13.Sep.00	29.38	8.80E+09	bd
AC63	205	ep, b?		22-Nov-00	31.94	1.40E+10	bd
AC70	290.5	ep, b	800	06.Nov.03	40.63	1.40E+10	pwr
AC71	185	ep	800	11.Dec.01	21.41	1.20E+10	bd
AC71	297.9	ep, b	800	12.Nov.04	40.66	1.10E+10	bd
AC71	461.3	ep, b	800	21.Feb.06	25.95	1.60E+10	bd
AC72	220	ep, b	1350	11.Feb.02	30.65	4.70E+09	bd
AC72	220	HPR	1350	27.May.03	37.11	5.50E+09	bd
Ac73	260	ep+, b	1350	14.Aug.02	35.5	8.60E+09	bd
AC75	247.5	ep	1350	31.Jul.02	23.05	1.50E+10	bd
AC75	165	ep+, b	800	09.Oct.02	35.06	9.30E+09	bd

Cavity							
AC76	213.4	ep, b	800	09.Nov.04	25.86	1.50E+10	bd
AC76	261.8	ep, b	800	24.May.05	35.39	1.50E+10	bd
AC76	261.8	HPR	800	04.Nov.05	33.57	9.20E+09	bd
AC78	262.5	ep, b	1350	21.Aug.02	36.34	9.10E+09	bd
AC78	298.5	ep, b	1350	07.Oct.03	24.35	2.90E+10	bd
AC80	327.5	ep, b	800	11.Mar.04	27.88	9.20E+09	bd
AC80	376.5	ep, b	800	30.Aug.04	27.71	1.30E+10	bd
AC81	292.9	ep	800	12.May.05	31.55	1.20E+10	bd
AC81	391.3	ep, b	800	13.Oct.05	35.27	9.80E+09	bd
AC115	204.4	ep, b	800	11.Dec.07	38.98	1.10E+10	bd
AC116	150	ep+, b	800	22.Feb.08	36.46	6.30E+09	bd
AC117	211.2	ep, b	800	14.Mar.08	39.53	1.10E+10	bd
AC118	153.8	ep+, b	800	14.Feb.08	30.36	1.50E+10	bd
AC119	226	ep+, b	800	06.Jun.08	24.77	1.50E+10	bd
AC120	182.8	ep, b	800	03.Jul.08	24.08	8.00E+09	bd
AC122	182	ep, b	800	26.Aug.08	38.88	9.50E+09	bd
AC123	174.4	ep+, b	800	06.Aug.08	31.48	7.80E+09	bd
AC125	158.4	ep, b	800	15.Jul.08	35.09	1.20E+10	bd
AC129	166	ep+, b	800	18.Jun.08	31.82	1.00E+10	bd
Z82	242.2	ep, b	800	15.Sep.04	28.91	1.50E+10	bd
Z83	240.4	ep, b	800	30.Sep.04	26.54	1.80E+10	bd
Z83	429.6	ep, b	1350	01.Nov.05	34.57	1.30E+10	bd
Z84	348.4	ep	800	12.Apr.05	27.7	1.40E+10	bd
Z85	240.8	ep, b	800	24.Mar.05	32.81	7.00E+09	bd
z86	241.2	ep, b	800	16.Sep.05	24.43	1.80E+10	bd
Z87	241.6	ep, b	800	28.Jun.05	33.25	1.20E+10	bd
Z88	258	ep	800	16.Jun.05	22.99	1.10E+10	bd
Z88	306.4	ep,b	800	25.Jul.07	32.03	1.30E+10	bd
Z89	241.2	ep, b	800	12.Aug.05	29.36	1.30E+10	bd
Z91	192.8	ep, b	800	15.Jan.07	30.16	1.30E+10	bd
Z93	242.4	ep, b	800	17.Apr.07	42.93	1.00E+10	bd
Z93	286	ep, b	800	03.Jul.07	40.15	9.90E+09	bd
Z95	193.6	ep, b	800	23.May.06	31.12	1.60E+10	bd
Z96	154.4	ep+	800	05.Jul.06	26.93	1.10E+10	bd
Z97	241.6	ep	800	30.May.07	26.05	1.60E+10	bd
Z98	154.8	ep+, b	800	10.Nov.06	31.4	8.70E+09	bd
Z99	156.8	ep+, b	800	26.Jul.06	31.4	5.60E+09	bd
Z100	304.4	ep, b	800	02.Jul.07	37.94	9.80E+09	pwr
Z101	230	ep, b	800	06.Mar.07	29.19	1.40E+10	bd
Z102	202.8	ep	800	23.Aug.06	26.62	1.50E+10	bd
Z103	175.6	ep. b	800	21.Sep.06	37.97	8.20E+09	bd
Z104	241.2	ep,b	800	20.Jun.07	37.44	9.80E+09	bd
Z105	159.2	ep+, b	800	31.Oct.06	18.33	8.70E+09	bd
Z105	207.6	ep, b	800	24.May.07	30.42	1.20E+10	bd
Z105	314.4	ep, b	800	30.May.08	29.25	1.20E+10	bd
Z106	192.8	ep, b	800	21.Feb.07	31.58	1.30E+10	bd

Z107	204.4	ep, b	800	16.Mar.07	33.07	1.10E+10	bd
Z108	193.2	ep	800	09.Jan.07	22.86	1.60E+10	bd
Z108	241.6	ep, b	800	10.Jul.07	33.13	1.20E+10	bd
Z109	154.4	ep+, b	800	11.Aug.06	26.48	8.30E+09	bd
Z019	207.8	ep, b	800	22.May.07	29.98	1.50E+10	bd
Z110	194.8	ep	800	07.Feb.07	14.76	1.30E+10	bd
Z111	154.8	ep+	800	24.Nov.06	16.15	1.80E+10	bd

Appendix B – List of DESY BCP tests (800°C) used in defect size statistical analysis
http://teslanew.desy.de/cavity_database/rf_tests/index_eng.html

Cavity	Removed Material [mu-m]	Cavity Status	HT [C]	Test Date	Max.Eacc [MV/m]	Qo @ Max.Eacc	Limitation
------	--------	------	---	---------	--------	--------	----------
AS4	80	bcp	800	11.Jun.98	20.57	8.20E+09	bd
AC71	202.5	bcp	800	08.Jul.02	31.16	3.70E+09	pwr
AC112	120	bcp	800	02.Nov.06	30.55	3.80E+09	bd
AC113	120	bcp	800	08.Nov.06	27.17	1.30E+10	bd
AC113	140	bcp	800	21.Mar.07	27.19	1.70E+10	bd
AC114	120	bcp	800	07.Jul.06	28.72	6.60E+09	bd
AC114	140	bcp	800	08.Mar.07	26.82	1.60E+10	bd
Ac117	162.8	bcp	800	27.Aug.07	31.31	9.00E+09	fe
C21	41.3	bcp	800	03.Mar.97	20.57	1.70E+10	bd
C24	191.3	bcp	800	06.Jan.98	18.88	6.90E+09	bd
C27	67.5	bcp	800	11.Feb.98	23.86	1.30E+10	bd
Z50	187.5	bcp	800	19.Apr.00	20.72	9.60E+09	bd
Z51	88.8	bcp	800	21.Mar.00	19.03	1.60E+10	bd
Z52	92.5	bcp	800	22.Feb.00	19.89	1.00E+10	bd
Z94	179.8	bcp	800	29.Jan.08	25.05	6.60E+09	bd
Z135	159	bcp	800	27.Aug.08	28.72	7.40E+09	bd

Appendix C – List of tests used in Q-slope data set
*http://teslanew.desy.de/cavity_database/rf_tests/index_*
eng.html

Cavity	Date
AC78	2-Oct-01
AC112	12-Dec-06
C21	20-Oct-05
C44	9-Dec-98
S31	11-Nov-98
S34	1-Sep-99
S35	15-Apr-03